

# Extending the Redox Potentials of Metal-Free Analytes: Towards High Energy Density Redox Flow Batteries

To cite this article: Jingchao Chai et al 2020 J. Electrochem. Soc. 167 100556

View the <u>article online</u> for updates and enhancements.







# **Extending the Redox Potentials of Metal-Free Analytes: Towards High Energy Density Redox Flow Batteries**

Jingchao Chai, Amir Lashgari, Xiao Wang, and Jianbing Jimmy Jiang Diang Diang

Department of Chemistry, University of Cincinnati, Cincinnati, Ohio 45221-0172, United States of America

Non-aqueous organic redox flow batteries (NORFBs) have emerged as a promising technology for renewable energy storage and conversion. High capacity and power density can be achieved by virtue of high solubility and high operating voltage of the organic anolytes and catholytes in organic media. However, the lack of anolyte materials with high redox potentials and their poor electrochemical stability retard the wider application of NORFBs. Here, we investigated an evolutionary design of a set of bipyridines and their analogues as anolytes and examined their performance in full flow batteries. Using combined techniques of repeated voltammetry, lower scan rate cyclic voltammetry, proton nuclear magnetic resonance, and density functional theory calculations, we could rapidly evaluate the redox potential, stability, and reversibility of these redox candidates. The promising candidates, 4-pyridylpyridinium bis(trifluoromethanesulfonyl)imide (monoMebiPy) and 4,4'-bipyridine (4,4'-biPy), were subjected to battery cycling. Extended studies of the post-cycling electrolytes were conducted to analyze the pathway of capacity fading and revealed a reduction-promoted methyl group shift mechanism for monoMebiPy. A family of easily accessible anolyte molecules with high redox stability and redox potentials was discovered that can be applied in NORFBs.

© 2020 The Electrochemical Society ("ECS"). Published on behalf of ECS by IOP Publishing Limited. [DOI: 10.1149/1945-7111/ab9e84]

Manuscript submitted April 5, 2020; revised manuscript received June 15, 2020. Published June 29, 2020.

Supplementary material for this article is available online

Renewable energy sources, such as solar and wind, are promising alternatives to mitigate the energy and environmental problems associated with fossil fuels. However, one of the key challenges of utilizing sustainable energy sources is to address their distinct intermittency. Smart grid is an attractive solution to address this problem. Under this circumstance, solving the issue of how to store and release electricity becomes a matter of urgency. Redox flow batteries (RFBs) have attracted widespread attention due to their cost-effectiveness and reliability. AFBs, the decoupled control of energy and power allows for the independent management of capacity and power to meet requirements for different applications. A10

Traditional RFBs, such as all-vanadium and Zn-Br RFBs, have reached a power/energy density in the scale of MW/MWh. 11-14 However, highly corrosive acid electrolytes such as H<sub>2</sub>SO<sub>4</sub> or KOH solutions<sup>15–19</sup> have to be employed, which ultimately causes maintenance, environmental, and cost concerns. Alternatively, considerable progress has been made with pH-neutral aqueous RFBs using organic electroactive compounds, in terms of high energy capacity, cyclability, and cost-effectiveness. 2,20,21,22-24 Nonetheless, the operating voltage of aqueous RFBs is limited by the narrow electrochemical window of aqueous electrolytes (<1.8 V). Recently, significant attention has been paid to non-aqueous organic RFBs (NORFBs). 6,26–35 Electrochemically stable organic solvents, such as carbonates, ethers, nitriles, and ionic liquids, have been widely applied in energy storage batteries, including lithium (metal), 36-42 sodium, 43,44 magnesium, 45,46 and aluminum ion batteries. 47–50 These electrolytes typically possess a wide electrochemical window (>4 V), making them suitable for applications in next-generation NORFBs.

The high potential of catholyte and anolyte is critical in NORFBs as it determines the overall cell voltage and power density. In recent years, remarkable progress has been made in potential tuning of catholytes in NORFBs, including (but not limited to) metallocenes, 2,2,6,6-tetramethylpiperidine-1-oxyl (TEMPO), phenothiazine, and cyclopropenium (Fig. 1A). <sup>2,6,28,32,33,35,51-56</sup> However, the lack of suitable anolyte materials with a highly negative potential has limited the further development of high-voltage NORFBs. The most extensively studied organic anolyte materials are quinone and viologen, with a redox potential less negative than -1.5 V vs

Ag/Ag<sup>+</sup>. With viologen as the analyte material, a battery potential of 0.7–1.7 V can be achieved, 11,23,25,57 ideal for aqueous RFBs, given the relatively narrow electrochemical window of water (<1.8 V). Considerable efforts have been made to explore the more negative potential regime. <sup>26,54,58,59</sup> Sanford et al. reported the evolutionary design of a series of pyridine compounds as anolytes in NORFBs, and proposed the decomposition pathways of the unstable pyridine-based anolyte materials. They tested the materials in asymmetric and symmetric RFBs. 26,54,60 Hansmann and co-workers presented pyridinium-carbene hybrids with high stabilities and reversibilities in H-cells.<sup>61</sup> Though compelling, the reported anolyte systems still suffered from tedious and multiple synthetic steps, low electrolyte concentration, and/or lack of full flow battery demonstration. In this study, we investigated the structure-function relationships and the electrochemical instability mechanisms of a set of bipyridines and bipyridinium derivatives using tools such as cyclic voltammetry (CV), proton nuclear magnetic resonance (<sup>1</sup>H NMR) spectroscopy, and density functional theory (DFT) calculations. The analyte candidates were further evaluated in full NORFBs with respect to concentration-dependent properties and capacity loss mechanisms.

# **Materials and Experimental Method**

*Materials and instrumentations.*—All chemical reagents were purchased as is unless otherwise noted. The NMR data were collected with a Bruker AV 400 MHz spectrometer using acetonitrile- $d_3$  as the solvent. Electrospray ionization-mass spectrometry (ESI–MS) analysis was performed on an Orbitrap Fusion Lumos mass spectrometer from Thermo Scientific Electrochemical performance and battery measurements were collected with a Bio-Logic VSP potentiostat. Rotating disk electrode (RDE) experiment was conducted with a CHI 760e potentiostat with a Pine modulated speed rotator.

*Electrochemical measurement.*—Cyclic voltammetry (CV) measurements were conducted in a three-electrode system: a glassy carbon (3 mm in diameter) as the working electrode, a Pt wire electrode was used as the counter electrode, and a Ag/silver nitrate (AgNO<sub>3</sub>) electrode with 0.01 M AgNO<sub>3</sub>/acetonitrile (ACN) solution reference electrode. The glassy carbon working electrode was polished with 0.05  $\mu$ m Al<sub>2</sub>O<sub>3</sub> before using. All the tests were conducted in an Ar-filled glovebox. A solution of 0.1 M tetrabuty-lammonium hexafluorophosphate (TBAPF<sub>6</sub>) in ACN with 5 mM

These authors contributed equally to this work.

<sup>&</sup>lt;sup>z</sup>E-mail: jianbing.jiang@uc.edu

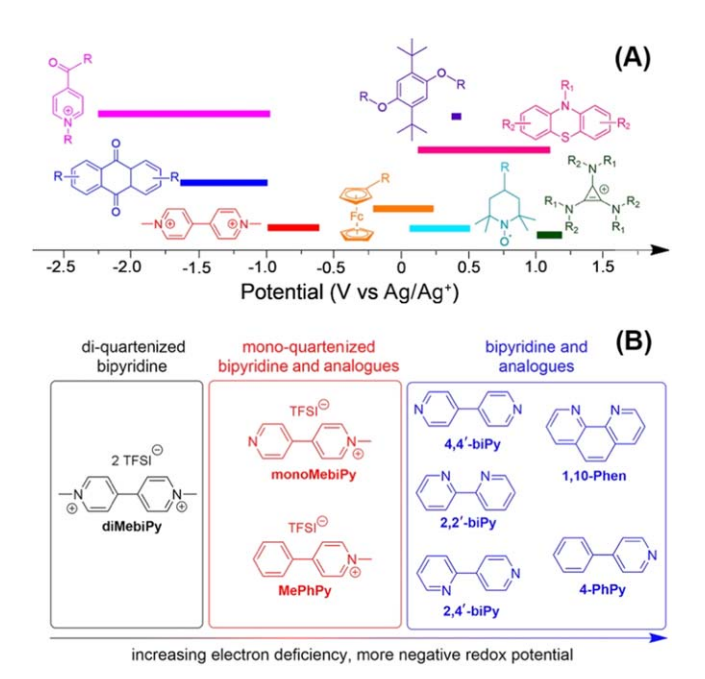


Figure 1. (A) Representative redox compounds in NORFBs. (B) Structures of bipyridines and analogues examined in this study.

sample was used as the testing electrolyte. All CV measurements were conducted using 5 mM sample in a 0.1 M TBAPF<sub>6</sub>-ACN solution. The bulk electrolysis of 5 mM compound is carried out in 0.1 M TBAPF<sub>6</sub>-ACN in a H-cell, where a Pt mesh, a graphite felt and a Ag/AgNO<sub>3</sub> electrode were used as the working electrode, counter electrode, and reference electrode, respectively. The schematic of an electrochemical H-cell is shown in Fig. S3.

*DFT calculation.*—All calculations were carried out using Gaussian  $09^{62}$  software for compounds at their original, one-electron and two-electron reduction states. All oxidation states were optimized at ground states with DFT and B3LYP/6-311 + G(d,p) basis set. The polarizable continuum model (PCM) was selected to optimize all geometries in ACN to include the solvation effect on free energies. The molecular orbital calculations were carried out with DFT method at B3LYP/6-311 + G(d,p) level.

Battery measurement.—A home-made flow cell was composed of Daramic membrane with an active surface area of 28 cm², sandwiched by two polytetrafluoroethylene frames. The graphite bipolar plate was placed on each side of the anode and cathode. 12 ml of 0.5 M TBAPF<sub>6</sub>-ACN with 50–240 mM active materials served as the electrolyte. The batteries were charged-discharged with galvanostatic technique. EIS measurements of the battery before and after cycling were tested in the glovebox with a 10-mV perturbation

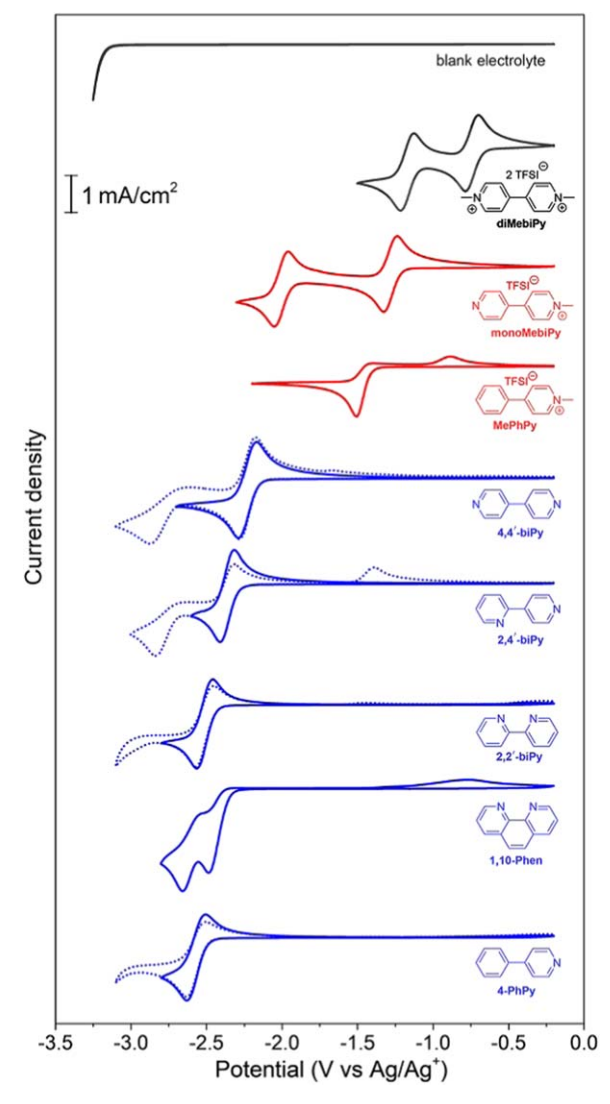


Figure 2. Cyclic voltammograms of bipyridines and their derivatives.

and with frequency ranging from 0.1 to 200,000 Hz at open circuit potential. CV scans of the electrolytes of the batteries after cycling were conducted in the glovebox. The electrolytes were diluted to one tenth with 0.1 M TBAPF<sub>6</sub>-ACN. The  $^1\mathrm{H}$  NMR samples were prepared using 400  $\mu\mathrm{L}$  electrolytes and 100  $\mu\mathrm{L}$  acetonitrile- $d_3$ .

## **Results and Discussion**

**Rationale.**—Our studies of bipyridines and their analogues started with CV, which serves as an effective tool to rapidly evaluate

Table I. Physical and electrochemical properties <sup>a)</sup> .							
Compound	Solubility <sup>b)</sup> (M)	$E_1(V)^{c)}$	Peak Separation for E <sub>1</sub> (mV)	$i_{\rm pc1}/i_{\rm pa1}$	$E_2(V)^{c)}$	Peak Separation for E <sub>2</sub> (mV)	$i_{\rm pc2}/i_{\rm pa2}$
diMebiPy	1.07	-0.82	85	1.05	-1.25	89	1.04
monoMebiPy	1.88	-1.28	92	1.03	-2.01	91	1.04
MePhPy	1.48	-1.45	_	_	_	_	
4,4'-biPy	1.05	-2.22	90	1.06	-2.78	_	_
2,4'-biPy	1.90	-2.36	88	1.05	-2.41	_	_
2,2'-biPy	1.61	-2.52	108	1.19	_	_	
1,10-Phen	1.51	-2.42	140	_	-2.60	_	_
4-PhPy	1.78	-2.57	113	1.35	_	_	_

a) All electrochemical measurements were conducted in 0.1 M TBAPF<sub>6</sub>-ACN at a concentration of 5 mM of analytes. b) In 0.1 M TBAPF<sub>6</sub>-ACN. c) All potentials are referenced to  $Ag/Ag^+$ .

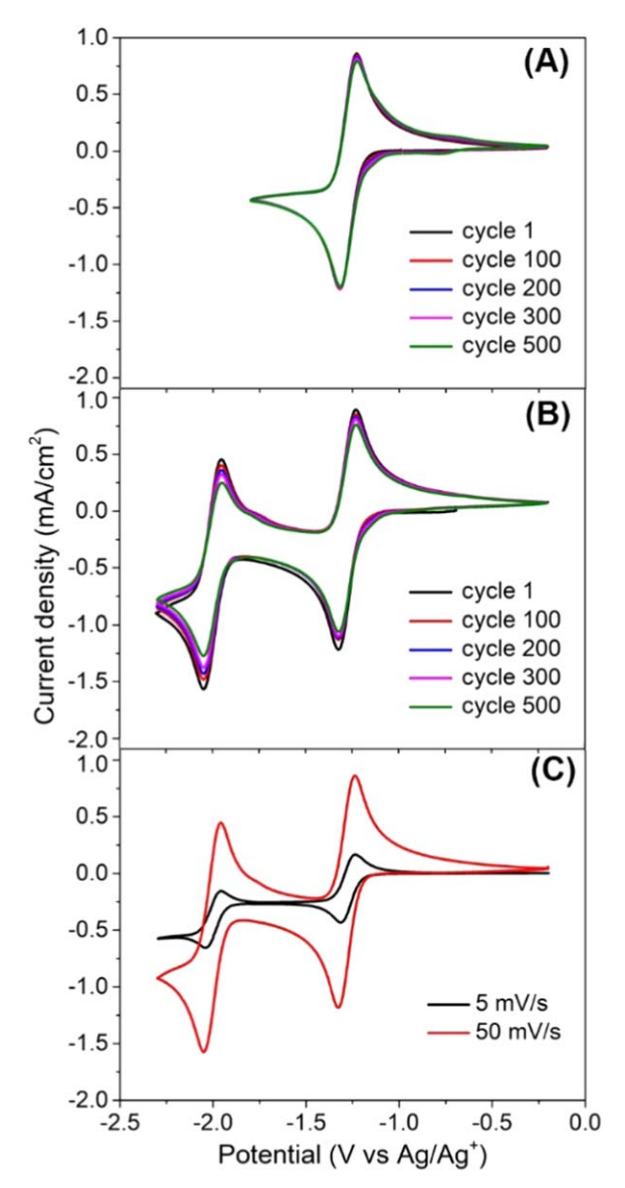


**Figure 3.** (A), (B) Repeat voltammograms of 5 mM **monoMebiPy** at  $50 \text{ m V s}^{-1}$ . (C) CV scans at  $50 \text{ mV s}^{-1}$  and  $5 \text{ m V s}^{-1}$ .

the redox potential and reversibility of the electroactive compounds and subsequently provide a feedback loop to design anolyte materials. The structure of di-quaternized bipyridine (with two positive charges), mono-quaternized bipyridine and analogues (with one positive charge), and bipyridine and analogues (electrically neutral), are illustrated in Fig. 1B.

All compounds examined here are either commercially available (4,4'-biPy, 2,4'-biPy, 2,2'-biPy, 1,10-Phen, and 4-PhPy), or can be synthesized in no more than two steps using inexpensive starting materials (diMebiPy, monoMebiPy, and MePhPy, see Supplementary Material for synthetic procedure and characterization data, Schemes S1 and S2, and Fig. S1 is available online at stacks.iop.org/JES/167/100556/mmedia). For quaternized compounds (diMebiPy, monoMebiPy, and MePhPy), the anions are all exchanged to bis(trifluoromethanesulfonyl) imide (TFSI) for high electrochemical stability and enhanced solubility. The solubility ranged between 1.05–1.90 M (Table I) in 0.1 M TBAPF<sub>6</sub>-ACN solution. corresponding to an energy capacity of 28.1–50.9 Ah 1<sup>-1</sup> for one-electron processes, making them suitable for flow battery application.

The di-quaternized bipyridine **diMebiPy**, commonly known as viologen, exhibits two characteristic redox couples at -0.82 V and -1.25 V vs  $Ag/Ag^+$  (Fig. 2, black), and the electrochemical

properties were widely studied in aqueous, 11,23,25,57,63,64 and recently non-aqueous RFBs. 28,65-69 However, for NORFB applications, it is imperative to further push the cathodic potential to take full advantage of the wide electrochemical window of non-aqueous electrolytes (> 4 V). 3,72 Compared to **diMebiPy**, the mono-quaternized analogue monoMebiPv exhibits two redox peaks at -1.28 V and -2.01 V vs Ag/Ag+ (Fig. 2, red), with a cathodic shift of 0.46 and 0.76 V for the first- and second-electron reduction events, respectively, due to the reduced electron-withdrawing effect. Additionally, the current peak-height ratios  $(i_{pc}/i_{pa})$  are close to 1 (Fig. 2 and Table I), suggesting full electrochemical reversibility. Once the pyridyl unit at the 4-position of **monoMebiPv** is replaced with phenyl (MePhPy) to increase the electron density of the diaryl system, one cathodic peak is observed at -1.45 V, but no corresponding reversible anodic peak is observed within the electrochemical window of ACN (Fig. 2, red). This is presumably because the phenyl unit is not as ideal a site for electron delocalization in the redox process as the pyridyl unit, where the electronegative N atom facilitates electron delocalization by stabilizing the resonant structures of the reduced compound.

Following the established molecular design principle of electron density tuning by varying the electronic properties of the N terminus, an even simpler structure 4.4'-biPv (Fig. 1B) was subjected to CV that displayed a reversible redox couple at -2.22 V vs Ag/Ag<sup>+</sup> (Fig. 2, blue), which is 210 mV lower in potential than that of the second redox couple of monoMebiPy. A tradeoff is that the second redox couple of 4,4'-biPy is quasi-reversible and only displays the reversible one-electron peak (Fig. 2), compared to the two-electron reversibility for the di- and mono-quaternized compounds. diMebiPv and monoMebiPv, respectively. We then examined the effect of varying the position of N atoms on the diaryl rings. The compound 2,4'-biPy displayed a reversible peak at -2.36 V vs Ag/Ag<sup>+</sup>, resulting in a 140-mV cathodic shift compared to 4,4'biPy. Moving both N atoms from the para to the ortho position (2,2'-biPy) further shifted the cathodic potential by 160 mV and afforded a redox potential at -2.52 V vs Ag/Ag<sup>+</sup>. The results were in accordance with DFT calculations; 4,4'-biPy possesses the highest lowest unoccupied molecular orbital (LUMO) among the three bipyridines (Fig. S2). All compounds displayed dihedral angles of ca. 37° according to DFT calculations. We then investigated compound 1,10-Phen with a co-planar geometry (dihedral angle of 0.026°). However, 1,10-Phen exhibited an irreversible peak at -2.42 V vs Ag/Ag<sup>+</sup> and a quasi-reversible peak at -2.60 V vs Ag/Ag<sup>+</sup>. Finally, one of the two N atoms of **4,4'-biPy** was replaced with carbon (4-PhPy) for higher electron density and afforded a reversible redox peak at -2.57 V vs Ag/Ag<sup>+</sup>, which is 350 mV lower than that of **4,4'-biPy** (-2.22 V vs Ag/Ag<sup>+</sup>). This result is consistent with the DFT calculation where compound 4-PhPy displayed a higher LUMO than the other four bipyridine counterparts (Fig. S2). The preliminary evaluation of the structurally modified analytes by CV and DFT calculation provided candidates with high redox potentials and reversibility for further examination.

**Electrochemical stability.**—The long-term stability of active materials is required for practical applications of RFBs. The methods employed to explore the long-term stability include (1) repeat CV scans at a scan rate of 50 mV s<sup>-1</sup>; and (2) CV scans using a low scan rate (5 m V s<sup>-1</sup>).<sup>26</sup> The one-electron redox properties of **monoMebiPy** were initially studied with repeat CV scans (Fig. 3A). The superimposed voltammetry curves after 500 cycles indicated a high-stability of **monoMebiPy** in the one-electron redox process. The same method was applied for the study of the two-electron redox process and showed minor intensity changes, with major redox characteristics retained after 500 cycles (Fig. 3B).

The chemical stability and reversibility of compounds can also be identified using voltammetry at a lower scan rate  $(5 \text{ m V s}^{-1})$ . The **monoMebiPy** compound exhibits a high chemical reversibility at  $5 \text{ mV s}^{-1}$  for both the one-electron  $(i_{pc}/i_{pa}=1.05)$  and two-electron  $(i_{pc}/i_{pa}=1.06)$  redox processes (Fig. 3C). Both the repeat and low

scan rate CV studies of monoMebiPy indicated that the monoquaternized structure has a high stability in the single- and doubleelectron redox process (Fig. 3). The electrochemical stability of 4,4'biPy, 2,4'-biPy, 2,2'-biBPy and 4-PhPy is examined using the same CV methods (Fig. 4). The highly superimposed CV curves of 4.4'biPv for 500 scan cycles confirmed its remarkable electrochemical stability (Fig. 4A). In addition, at a lower scan rate of 5 mV s<sup>-1</sup>, the almost identical anodic and cathodic current densities of 4,4'-biPy  $(i_{\rm pc}/i_{\rm pa}=1.06,\,{\rm Fig.~4B})$  support the conclusion from the repeat CV study. Although CV scans of 2,4'-biPy show a slight intensity decrease after 500 cycles (Fig. 4C), the  $i_{pc}/i_{pa}$  ratio at 5 mV s<sup>-1</sup> is 1.02 (Fig. 4D), the significant reversibility and electrochemical stability are evident. By contrast, the compound 2,2'-biPy presents poor repeatability after 500 CV cycles (Fig. 4E) and its low-scan rate study does not present the anodic peak (Fig. 4F). The poor chemical stability of 4-PhPy is also observed (Figs. 4G and 4H). The longterm stability study revealed subtle structural variations (N vs C atoms for 4.4'-biPv and 4-PhPv; and para- vs ortho- for 4.4'-biPv, 2,4'-biPy, 2,2'-biPy).

**Battery performance.**—The promising anode candidates **4,4'-biPy** and **monoMebiPy** were further evaluated in full NORFBs. The galvanostatic charge/discharge measurement was conducted to fully assess the electrochemical performance in an RFB system. The PEGylated phenothiazine (**PEG12-PTZ**) was used as catholyte material owing to its excellent electrochemical performance. For **monoMebiPy** and **4,4'-biPy**, the corresponding potentials and representative half-cell reactions of a non-aqueous RFB are illustrated in Fig. 5. The bipyridine analogues-based RFBs present a theoretical working potential ranging from 1.67 to 2.61 V (Fig. 5A), much higher than that of the viologen counterparts. <sup>70,10,15,16,71,72</sup> Mixed-reactant electrolytes are employed using Daramic membranes to separate the anolyte and catholyte sides. The catholyte material is used in excess to ensure full utilization of the anolyte. A variety of concentrations (50–240 mM) were investigated to probe the concentration-dependent performance.

The discharge capacity and Coulombic efficiency of NORFBs with 50 mM **4,4'-biPy** and **monoMebiPy** are presented in Fig. 6A. The **4,4'-biPy/PEG12-PTZ** battery displays an open circuit potential of 2.64 V at fully-charged state and an initial discharge capacity of 9.29 mAh at a current density of 50 mA cm<sup>-2</sup> (Fig. 6B). After

40 cycles, the RFB delivers a capacity retention of 70.0%, corresponding to a loss of 0.75% per cycle with an average Coulombic efficiency of 89.6%. The CV scans of post-cycling electrolytes show that the anolyte curve is similar to that of the electrolyte before cycling, indicating the high stability of 4,4'-biPy and PEG12-PTZ on the anolyte side (Fig. 6C). However, unexpected redox peaks appear on the catholyte side, implying the presence of new species. As PEGylated phenothiazine provided high stability and reversibility in NORFBs<sup>31,52,73</sup> and **4,4'-biPy** is electrochemically stable under reducing conditions, we hypothesized that the poor performance of 4,4'-biPy/PEG12-PTZ RFB is mainly related to the instability of **4.4'-biPv** at positive potentials. To evaluate the stability of **4.4'-biPv** at positive potentials, 5 mM of 4,4'-biPy is bulk electrolyzed for 5 h at 0.4 V vs Ag/Ag<sup>+</sup> in a H-cell (Fig. S3). The CV of the resulting 4,4'-biPy solution revealed two additional peaks at -1.25 and -0.75 V (Fig. S4). In parallel to the bulk electrolysis study, repeated CV scans are also conducted in a three-electrode configuration with potentials ranging from -2.4 to 0.8 V (Fig. S5). The anodic peak gradually disappeared over the course of the 500-cycle scans. Furthermore, an additional peak gradually emerged at -1.2 V. Both the bulk electrolysis and repeated CV scan experiment indicated that **4,4'-biPy** is instable at positive potentials, which agrees with the battery results. The post-cycling electrolytes of the 4,4'-biPy/ **PEG12-PTZ** RFB are also studied by <sup>1</sup>H NMR (Fig. S6), which shows the presence of extra species in the catholyte, demonstrating the instability of **4.4'-biPy** at high positive voltage. The broadened <sup>1</sup>H NMR signals (Fig. S6) indicated the possible oxidative polymerization of pyridine units at positive potentials.<sup>7</sup>

Under the same battery test conditions, the capacity retention of the **monoMebiPy/PEG12-PTZ** battery after 250 cycles is 76.6%, indicating a capacity loss of 0.09% per cycle (Fig. 6A, red). The initial discharge capacity is 9.96 mAh (Fig. 6D), corresponding to 61.9% of the theoretical value. During the 250 cycles of charging/discharging, the Coulombic, energy, and voltage efficiencies of the battery are 94.6%, 55.8%, and 57.0%, respectively. The representative charge/discharge profiles of the **monoMebiPy/PEG12-PTZ** battery from 0.8 to 2.3 V are presented in Fig. 4D. The gradually increasing overpotential of the battery is correlated to the enhanced specific area resistance (Fig. S7). Nevertheless, the **monoMebiPy/PEG12-PTZ** battery still provided steady charge/discharge properties over 250 cycles.

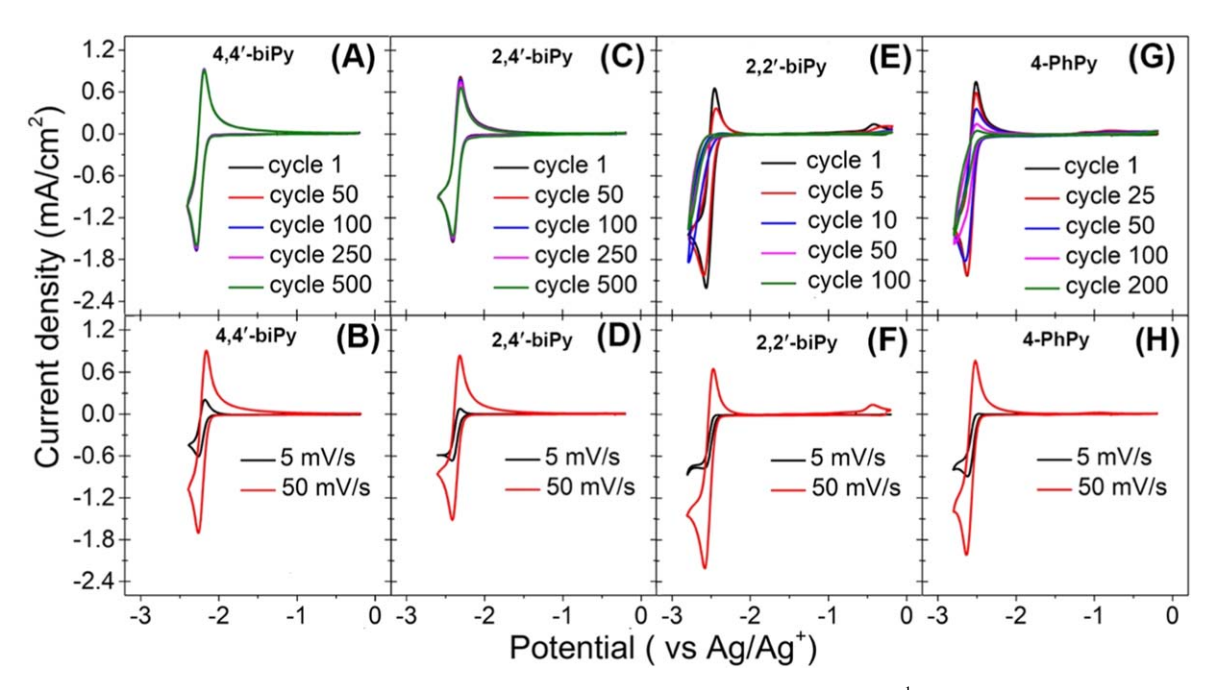


Figure 4. Repeat voltammograms of (A) 4,4'-biPy, (C) 2,4'-biPy, (E) 2,2'-biPy and (G) 4-PhPy at 50 m V s<sup>-1</sup>. CV scans of (B) 4,4'-biPy, (D) 2,4'-biPy, (F) 2,2'-biPy and (H) 4-PhPy at 50 mV s<sup>-1</sup> and 5 m V s<sup>-1</sup>.

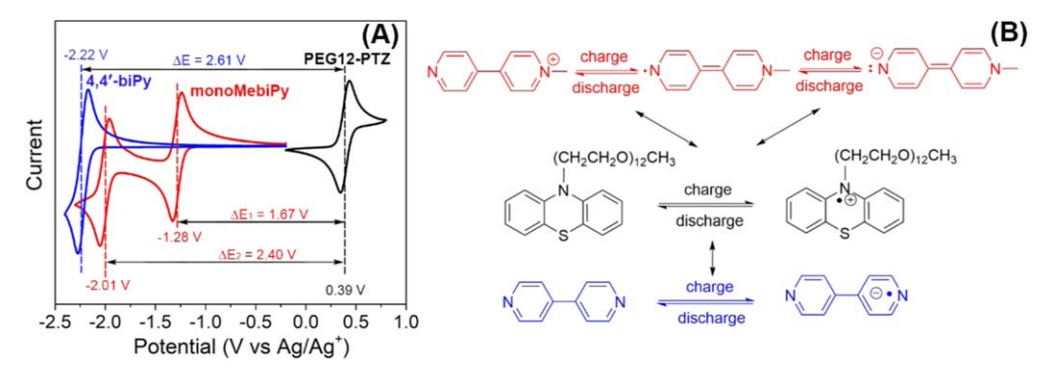


Figure 5. (A) CV scans of anolyte and catholyte compounds in 0.1 M TBAPF<sub>6</sub>-ACN. (B) Half-cell reactions and corresponding redox potentials.

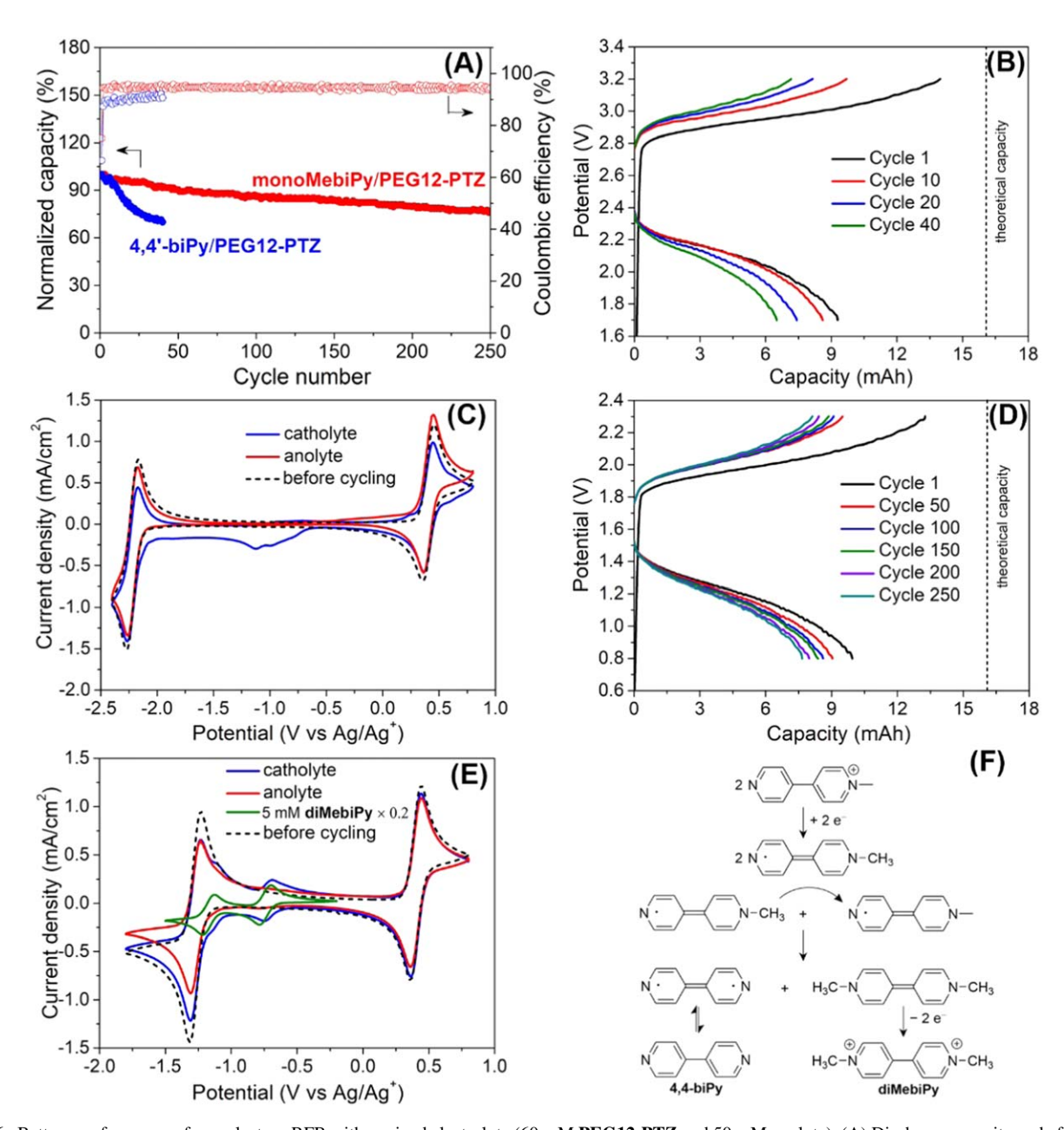


Figure 6. Battery performance of one-electron RFB with a mixed electrolyte (60 mM PEG12-PTZ and 50 mM anolyte). (A) Discharge capacity and efficiencies vs cycle number. Representative charge/discharge curves at different cycle number of (B) 4,4'-biPy/PEG12-PTZ and (D) monoMebiPy/PEG12-PTZ batteries. CV scans of the post-cycling electrolytes of (C) 4,4'-biPy/PEG12-PTZ and (E) monoMebiPy/PEG12-PTZ batteries. (F) Reduction-promoted methyl shift mechanism for diMebiPy formation in catholyte.

To explore the capacity loss mechanism of the monoMebiPy/ PEG12-PTZ battery, the post-cycling electrolytes are analyzed by CV (Fig. 6E) and <sup>1</sup>H NMR spectroscopy (Fig. S8). The analyte demonstrates a stable CV curve without any additional redox peaks. In addition, the one-electron reaction of monoMebiPy has almost no effect on the reversible two-electron activity (Fig. S9). However, two additional reversible redox peaks at -0.72 V and -1.13 V were observed in the catholyte, which are characteristic of bipyridinium diMebiPy. The bipyridinium diMebiPy is presumably formed via a reduction-promoted methyl shift mechanism (Fig. 6F). No distinct redox peak of 4,4'-biPy is observed in the CV of the post-cycling catholyte (Fig. S10), probably because of the decomposition of 4,4'**biPy** at positive potentials, which has been confirmed with analysis of the electrolytes of the 4,4'-biPy/PEG12-PTZ battery. To confirm whether the reduction of monoMebiPy is required for the methyl shift process, bulk electrolysis of monoMebiPy was carried out at a positive potential (0.4 V vs Ag/Ag<sup>+</sup>). The CV of the electrolyzed monoMebiPy was monitored at various time periods, but no diMebiPy peaks were observed (Fig. S11). The CV result indicated that monoMebiPy in its neutral charge state is stable at positive potentials and does not undergo methyl shift reactions, which was also confirmed by <sup>1</sup>H NMR (Fig. S12).

To enhance the energy density of a non-aqueous RFB, a battery at a higher concentration (200 mM monoMebiPv and 240 mM **PEG12-PTZ** in 0.5 M TBAPF<sub>6</sub>-ACN) was galvanostatically charged/discharged at a current density of 50 mA cm<sup>-2</sup>. The volume change of the electrolyte solution caused by osmotic pressure has a significant effect on the battery performance (Fig. S13). The volume change can be suppressed by adjusting the flow rate. At an optimal flow rate (100 rpm for anolyte and 104 rpm for catholyte), the discharge capacity of this battery is  $4.16 \text{ Ah } 1^{-1}$ , 77.4% of the theoretical capacity. After 39 charge/discharge cycles, a capacity of 2.91 Ah l<sup>-1</sup> is obtained, corresponding to a 70.1% capacity retention (Fig. 7A). Compared to the battery with a monoMebiPy concentration of 50 mM (Fig. 6A, red), this battery provides a lower Coulombic efficiency (86.8% vs 94.6%), but a higher voltage efficiency (62.8% vs 57.0%). Despite the gradual loss of the discharge capacity, the charge/discharge profiles are stable throughout the cycling study (Fig. 7B). The CV scans of electrolytes after 39 cycles indicated that the decomposition of **monoMebiPy** in the catholyte is more severe than that in the battery with lower electrolyte concentration (Fig. 7C), which is caused by the bimolecular methyl group shift at higher concentration. Moreover, there were additional small redox peaks in the anolyte, which might have resulted from the crossover of decomposed **monoMebiPy** from catholyte.

To enhance the energy and power density of the monoMebiPy/ PEG12-PTZ battery, the second electron of monoMebiPv was utilized. As a starting point to utilize two electrons of monoMebiPv. a non-aqueous RFB with a low electrolyte concentration (10 mM monoMebiPy and 25 mM PEG12-PTZ) was investigated. The battery was initially galvanostatically charged/discharged at 20 mA cm<sup>-2</sup>, with a potential ranging from 1.0 to 2.2 V (Fig. 8A) for one-electron utilization. Stable cyclability for 5 cycles was observed. When the battery was charged to 2.8 V for two-electron utilization, the battery presented a doubled charging capacity, indicating the successful two-electron redox process (6th cycle in Fig. 8B). Unfortunately, the discharge capacity at the sixth cycle decreased dramatically (Fig. 8B), resulting in a Coulombic efficiency of 40.3%. In the following cycling, the capacity of the monoMebiPv/PEG12-PTZ battery rapidly faded and low Coulombic efficiencies were observed. After 12 cycles the electrolytes were subjected to CV and <sup>1</sup>H NMR studies. The catholyte shows a curve similar to that of the one-electron RFB (Fig. 8C), further confirming the high electrochemical stability of PEG12-PTZ. However, the analyte displayed unexpected redox features, which are attributed to side reactions between the doubly reduced monoMebiPv and PEG12-PTZ (Figs. S14 and S15).

To investigate the unusual electrochemical behavior of the anolyte and the stability of **monoMebiPy** in a wider electrochemical window, repeated CV scans of 5 mM **monoMebiPy** including the positive potential regime were conducted. It is observed that **monoMebiPy** exhibits undesirable cyclability in the potential ranging from -2.3 to 0.8 V, especially for the second-reduction process (Fig. 8D, top). The two-electron redox property of **monoMebiPy** almost disappeared at the 100th cycle, though

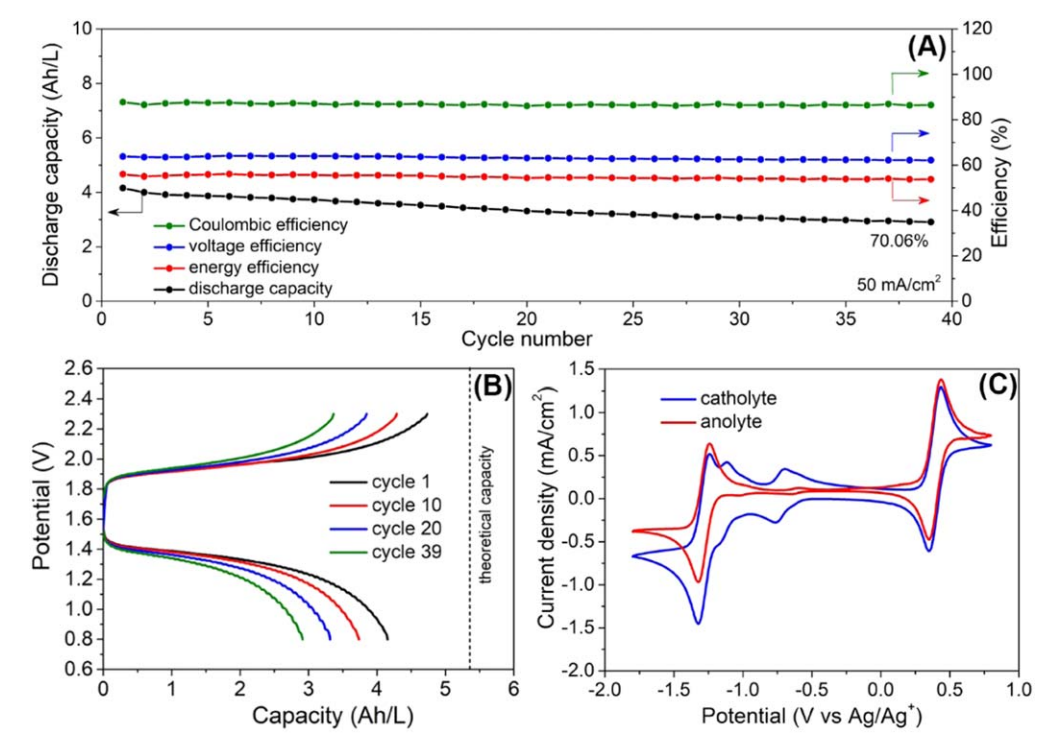


Figure 7. RFB with mixed electrolytes of 200 mM monoMebiPy and 240 mM PEG12-PTZ. (A) Discharge capacity and efficiencies vs cycle number. (B) Representative charge/discharge curves at different cycle numbers. (C) CV scans of electrolytes after cycling.

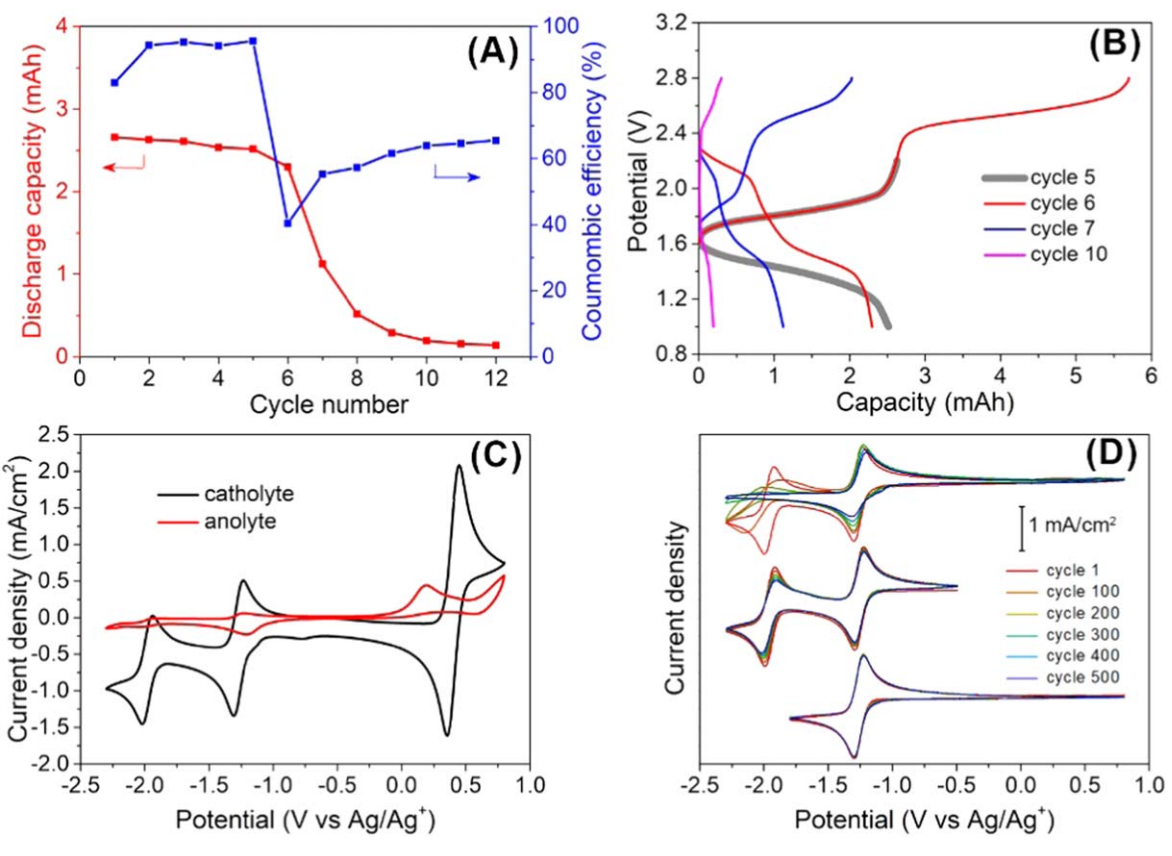


Figure 8. Battery performance of two-electron utilization with a mixed electrolyte (25 mM PEG12-PTZ and 10 mM monoMebiPy). (A) Discharge capacity and Coulombic efficiency vs cycle number. (B) Representative charge/discharge curves of the battery at different cycle number. (C) CV scans of electrolytes after 12 cycles. (D) Repeated CV scans of 5 mM monoMePhPy in 0.1 M TBAPF<sub>6</sub>-ACN in different potential range at a scan rate of 50 mV s<sup>-1</sup>. The CV ranging from -2.3 to -0.2 V in panel D is duplicated from Fig. 2B for direct comparison.

monoMebiPy presents adequate cyclability in CV scans in the potential ranging from -2.3 to -0.2 V (Fig. 8D middle). Moreover, monoMebiPv is stable in the potential ranging from -1.8 to 0.8 V, where the two-electron reduction process is precluded (Fig. 8D bottom). Altogether, the monoMebiPy analyte was electrochemically stable for one-electron reduction in a wide electrochemical window (-1.8 to 0.8 V), and for two-electron reduction in a negative potential window (-2.3 to -0.2 V). Therefore, for the practical application of these pyridine-based analyte materials, it is essential to explore functional membranes to separate the catholyte and anolyte materials avoiding the overoxidation of anolyte.

#### **Conclusions**

In summary, a set of bipyridine, bipyridiniums, and their derivatives was explored as anolyte materials for NORFBs. All compounds examined in this study were either commercially available and inexpensive or can be synthesized in less than two steps. A combination of voltammetry, spectroscopy, computation, and battery tests guided the evaluation of the anolytes. The iterative structural verification of the bipyridine compounds afforded compound 4-PhPy with the most negative potential of -2.57 V vs Ag/Ag<sup>+</sup>. The compounds monoMebiPy and 4,4'-biPy displayed stable battery cycling using phenothiazine as the catholyte. The mechanistic findings provided insights into the side reactions of the mono-quaternized monoMebiPy under reducing conditions. Overall, the bipyridine compounds described herein delivered a promising family of NORFB anolytes and revealed insights into molecular designs of other pyridinium compounds. Our ongoing work explores asymmetric battery systems with mitigated resistance to allow anolyte studies at higher concentrations.

### Acknowledgments

The authors acknowledge the University of Cincinnati for startup funding support, and Ohio Supercomputer Center for providing the computational resources. NMR experiments were performed on a Bruker AVANCE NEO 400 MHz NMR spectrometer funded by NSF-MRI grant CHE-1726092.

#### **ORCID**

Amir Lashgari https://orcid.org/0000-0001-5976-4871 Jianbing "Jimmy" Jiang https://orcid.org/0000-0002-7466-522X

#### References

- 1. R. Yan and Q. Wang, Adv. Mater., 30, 1802406 (2018).
- J. Winsberg, T. Hagemann, T. Janoschka, M. D. Hager, and U. S. Schubert, *Angew*. Chem. Int. Ed., 56, 686 (2017).
- 3. Y. Ding, C. Zhang, L. Zhang, Y. Zhou, and G. Yu, Chem. Soc. Rev., 47, 69 (2018).
- 4. J. Luo, B. Hu, M. Hu, Y. Zhao, and T. L. Liu, ACS Energy Lett., 4, 2220 (2019).
- 5. W. Li, H. C. Fu, L. Li, M. Cabán Acevedo, J. H. He, and S. Jin, Angew. Chem. Int. Ed., 55, 13104 (2016).
- C. Zhang, Y. Qian, Y. Ding, L. Zhang, X. Guo, Y. Zhao, and G. Yu, Angew. Chem. Int. Ed., 131, 119 (2019).
- Y. Ding and G. Yu, Angew. Chem. Int. Ed., 56, 8614 (2017).
- 8. D. G. Kwabi, Y. Ji, and M. J. Aziz, Chem. Rev., (2020).
- C. Zhang, Y. Ding, L. Zhang, X. Wang, Y. Zhao, X. Zhang, and G. Yu, Angew. Chem. Int. Ed., 56, 7454 (2017).
- K. Lin, Q. Chen, M. R. Gerhardt, L. Tong, S. B. Kim, L. Eisenach, A. W. Valle, D. Hardee, R. G. Gordon, and M. J. Aziz, Science, 349, 1529 (2015).
- 11. C. DeBruler, B. Hu, J. Moss, X. Liu, J. Luo, Y. Sun, and T. L. Liu, Chem, 3, 961 (2017).
- 12. B. Dunn, H. Kamath, and J. M. Tarascon, Science, 334, 928 (2011).
- 13. Z. Yang, J. Zhang, M. C. Kintner-Meyer, X. Lu, D. Choi, J. P. Lemmon, and J. Liu, Chem. Rev., 111, 3577 (2011).
- 14. Q. Huang and Q. Wamng, ChemPlusChem, 80, 312 (2015).

- 15. P. X. Han, H. B. Wang, Z. H. Liu, X. A. Chen, W. Ma, J. H. Yao, Y. W. Zhu, and G. L. Cui, Carbon, 49, 693 (2011).
- 16. P. X. Han, Y. H. Yue, Z. H. Liu, W. Xu, L. X. Zhang, H. X. Xu, S. M. Dong, and G. L. Cui, Energy Environ. Sci., 4, 4710 (2011).
- 17. W. O. Liu, W. J. Lu, H. M. Zhang, and X. F. Li, *Chem. Eur. J.*, **25**, 1649 (2019).
- 18. X. F. Li, H. M. Zhang, Z. S. Mai, H. Z. Zhang, and I. Vankelecom, *Energy Environ*. Sci 4 1147 (2011)
- 19. Z. Z. Yuan, Y. Q. Duan, H. Z. Zhang, X. F. Li, H. M. Zhang, and I. Vankelecom, Energy Environ. Sci., 9, 441 (2016).
- 20. B. H. Hu, J. L. Luo, M. Hu, B. Y. Yuan, and T. L. Liu, Angew. Chem. Int. Ed., 58, 16629 (2019).
- 21. J. Luo, B. Hu, C. Debruler, Y. Bi, Y. Zhao, B. Yuan, M. Hu, W. Wu, and T. L. Liu, Joule, 3, 149 (2019).
- 22. S. Jin, Y. Jing, D. G. Kwabi, Y. Ji, L. Tong, D. De Porcellinis, M.-A. Goulet, D. A. Pollack, R. G. Gordon, and M. J. Aziz, ACS Energy Lett., 4, 1342 (2019).
- 23. B. Hu, C. DeBruler, Z. Rhodes, and T. L. Liu, J. Am. Chem. Soc., 139, 1207 (2017).
- 24. J. Luo, B. Hu, C. Debruler, and L. T. Leo, Angew. Chem. Int. Ed., 57, 231 (2018).
- 25. J. Luo, W. Wu, C. R. DeBruler, B. Hu, M. Hu, and T. Liu, J. Mater. Chem. A, 7, 9130 (2019)
- 26. C. S. Sevov, R. E. Brooner, E. Chenard, R. S. Assary, J. S. Moore, J. Rodríguez-López, and M. S. Sanford, J. Am. Chem. Soc., 137, 14465 (2015).
- P. J. Cabrera, X. Yang, J. A. Suttil, K. L. Hawthorne, R. E. M. Brooner, M. S. Sanford, and L. T. Thompson, *J. Phys. Chem. C*, 119, 15882 (2015).
- 28. B. Hu and T. L. Liu, J. Energy Chem., 27, 1326 (2018).
- 29. C. Zhang, Z. Niu, Y. Ding, L. Zhang, Y. Zhou, X. Guo, X. Zhang, Y. Zhao, and G. Yu, Chem, 4, 2814 (2018).
- 30. Y. Ding, Y. Zhao, Y. Li, J. B. Goodenough, and G. Y. Yu, Energy Environ. Sci., 10, 491 (2017)
- 31. J. D. Milshtein et al., Energy Environ. Sci., 9, 3531 (2016).
- 32. S. O. Tung, S. L. Fisher, N. A. Kotov, and L. T. Thompson, Nat. Commun., 9, 4193 (2018).
- 33. T. Ma, Z. Pan, L. Miao, C. Chen, M. Han, Z. Shang, and J. Chen, Angew. Chem. Int. Ed., 57, 3158 (2018).
- 34. X. Wei et al., ACS Energy Lett., 2, 2187 (2017)
- 35. X. Wei et al., Angew. Chem. Int. Ed., 54, 8684 (2015).
- 36. Q. Zhou, J. Ma, S. Dong, X. Li, and G. Cui, Adv. Mater., 31, 1902029 (2019).
- 37. G. Xu, X. Shangguan, S. Dong, X. Zhou, and G. Cui, Angew. Chem. Int. Ed., 59, 3400 (2020).
- 38. K. Liang, K. Marcus, S. Zhang, L. Zhou, Y. Li, S. T. De Oliveira, N. Orlovskaya,
- Y. H. Sohn, and Y. Yang, Adv. Energy Mater., 7, 1701309 (2017).
   L. Wang, K. Liang, G. Wang, and Y. Yang, J. Mater. Chem. A, 6, 13968 (2018).
- 40. Y. Yang, Y. Zhong, Q. Shi, Z. Wang, K. Sun, and H. Wang, Angew. Chem. Int. Ed., **130**, 15775 (2018).
- 41. Y. Zhong, L. Yin, P. He, W. Liu, Z. Wu, and H. Wang, J. Am. Chem. Soc., 140, 1455 (2018).
- 42. Q. Shi, Y. Zhong, M. Wu, H. Wang, and H. Wang, Proc. Natl Acad. Sci. USA, 115, 5676 (2018).
- 43. Y. S. Hu and Y. X. Lu, ACS Energy Lett., 4, 2689 (2019).
- 44. Z. Xu, F. Xie, J. Wang, H. Au, M. Tebyetekerwa, Z. Y. Guo, S. Y. Yang, Y. S. Hu, and M. M. Titirici, Adv. Funct. Mater., 29, 1903895 (2019).
- 45. A. B. Du, H. R. Zhang, Z. H. Zhang, J. W. Zhao, Z. L. Cui, Y. M. Zhao, S. M. Dong, L. L. Wang, X. H. Zhou, and G. L. Cui, Adv. Mater., 31, 1805930 (2019)
- 46. A. B. Du et al., Energy Environ. Sci., 10, 2616 (2017).

- 47. M. Lin et al., Nature, 520, 324 (2015).
- 48. Y. P. Wu et al., Adv. Mater., 28, 9218 (2016).
- 49. M. Angell, C. J. Pan, Y. M. Rong, C. Z. Yuan, M. C. Lin, B. J. Hwang, and H. J. Dai, Proc. Natl Acad. Sci. USA, 114, 834 (2017).
- 50. K. Liang, L. Ju, S. Koul, A. Kushima, and Y. Yang, Adv. Energy Mater., 9, 1802543 (2019)
- 51. X. Wei, W. Duan, J. Huang, L. Zhang, B. Li, D. Reed, W. Xu, V. Sprenkle, and W. Wang, ACS Energy Lett., 1, 705 (2016).
- 52. J. A. Kowalski et al., J. Mater. Chem. A, 5, 24371 (2017).
- 53. Y. Yan, S. G. Robinson, M. S. Sigman, and M. S. Sanford, J. Am. Chem. Soc., 141, 15301 (2019).
- 54. C. S. Sevov, D. P. Hickey, M. E. Cook, S. G. Robinson, S. Barnett, S. D. Minteer, M. S. Sigman, and M. S. Sanford, J. Am. Chem. Soc., 139, 2924 (2017).
- 55. C. S. Sevov, S. K. Samaroo, and M. S. Sanford, Adv. Energy Mater., 7, 1602027
- 56. K. H. Hendriks, S. G. Robinson, M. N. Braten, C. S. Sevov, B. A. Helms, M. S. Sigman, S. D. Minteer, and M. S. Sanford, ACS Cent. Sci., 4, 189 (2018).
- 57. E. S. Beh, D. De Porcellinis, R. L. Gracia, K. T. Xia, R. G. Gordon, and M. J. Aziz, ACS Energy Lett 2 639 (2017)
- 58. G. Wang, B. Huang, D. Liu, D. Zheng, J. Harris, J. Xue, and D. Qu, J. Mater. Chem. A 6 13286 (2018)
- 59. S. G. Robinson and M. S. Sigman, Acc. Chem. Res., 53, 289 (2020).
- 60. M. Sanford, A. Shrestha, K. Hendriks, M. Sigman, and S. Minteer, Chem. Eur. J., (2020).
- 61. P. W. Antoni, T. Bruckhoff, and M. M. Hansmann, J. Am. Chem. Soc., 141, 9701 (2019).
- 62. M. J. Frisch et al., Gaussian 09 (Gaussian Inc, Wallingford, CT) (2009)
- 63. T. Liu, X. Wei, Z. Nie, V. Sprenkle, and W. Wang, Adv. Energy Mater., 6, 1501449 (2016).
- Y. Liu, M. A. Goulet, L. Tong, Y. Liu, Y. Ji, L. Wu, R. G. Gordon, M. J. Aziz, Z. Yang, and T. Xu, Chem, 5, 1861 (2019).
- 65. E. C. Montoto, G. Nagarjuna, J. S. Moore, and J. Rodríguez-López, J. Electrochem. Soc., 164, A1688 (2017).
- G. Nagarjuna, J. Hui, K. J. Cheng, T. Lichtenstein, M. Shen, J. S. Moore, and J. Rodríguez-López, J. Am. Chem. Soc., 136, 16309 (2014).
- 67. M. Burgess, J. S. Moore, and J. Rodríguez-López, Acc. Chem. Res., 49, 2649 (2016)
- 68. M. Burgess, E. Chénard, K. Hernández-Burgos, G. Nagarjuna, R. S. Assary, J. Hui, J. S. Moore, and J. Rodríguez-López, *Chem. Mater.*, 28, 7362 (2016).
- 69. M. Burgess, K. Hernández-Burgos, B. H. Simpson, T. Lichtenstein, S. Avetian, G. Nagarjuna, K. J. Cheng, J. S. Moore, and J. Rodríguez-López, J. Electrochem. Soc., 163, H3003 (2016).
- 70. B. Huskinson, M. P. Marshak, C. Suh, S. Er, M. R. Gerhardt, C. J. Galvin, X. Chen, A. Aspuru-Guzik, R. G. Gordon, and M. J. Aziz, Nature, 505, 195 (2014).
- 71. A. Orita, M. G. Verde, M. Sakai, and Y. S. Meng, Nat. Commun., 7, 13230 (2016).
- 72. A. Hollas, X. Wei, V. Murugesan, Z. Nie, B. Li, D. Reed, J. Liu, V. Sprenkle, and W. Wang, Nat. Energy, 3, 508 (2018).
- 73. N. H. Attanayake, J. A. Kowalski, K. V. Greco, M. D. Casselman, J. D. Milshtein, S. J. Chapman, S. R. Parkin, F. R. Brushett, and S. A. Odom, Chem. Mater., 31, 4353 (2019).
- 74. I. M. F. De Oliveira and J. C. Moutet, J. Electrochem. Soc., 361, 203 (1993).
- 75. M. Pardo, J. Perez, M. del Valle, M. Godoy, and F. Diaz, J. Chil. Chem. Soc., 59, 2464 (2014).